Strain-Controlled Low Cycle Fatigue Properties of a Rare-Earth Containing ZEK100 Magnesium Alloy

F. Mokdad, D.L. Chen

PII: S0261-3069(14)00980-7
DOI: http://dx.doi.org/10.1016/j.matdes.2014.11.058
Reference: JMAD 7010

To appear in: *Materials and Design*

Received Date: 17 September 2014
Accepted Date: 29 November 2014

Please cite this article as: Mokdad, F., Chen, D.L., Strain-Controlled Low Cycle Fatigue Properties of a Rare-Earth Containing ZEK100 Magnesium Alloy, *Materials and Design* (2014), doi: http://dx.doi.org/10.1016/j.matdes.2014.11.058

Strain-Controlled Low Cycle Fatigue Properties of a Rare-Earth Containing ZEK100 Magnesium Alloy

F. Mokdad and D.L. Chen*

Department of Mechanical and Industrial Engineering, Ryerson University,

350 Victoria Street, Toronto, Ontario M5B 2K3, Canada

Abstract

Low rare-earth (RE) containing magnesium alloys are being considered for the lightweight automotive applications to reduce fuel consumption and emissions. Design of magnesium components requires strain-controlled low-cycle fatigue (LCF) behavior. This study was aimed to evaluate the cyclic deformation characteristics and LCF life of a low (0.2 wt.%) Nd-containing ZEK100-O alloy. The alloy contained equiaxed grains along with some $Mg_{12}Nd$ particles, and exhibited a relatively weaker basal texture. While slight cyclic softening occurred at high strain amplitudes, cyclic stabilization remained at lower strain amplitudes. Fatigue life of ZEK100 alloy was longer than that of the extruded RE-free AZ31 and AM30 alloys, due to a fairly good combination of strength with ductility. The asymmetry and skewness of hysteresis loops, which were characterized by eccentricity, angle deviation, and relative slope change, respectively, were effectively improved relative to the extruded RE-free alloys, arising from less extensive twinning

---

*Corresponding author – Tel: (416) 979-5000 ext. 6487; Fax: (416) 979-5265; Email: dchen@ryerson.ca (D.L. Chen).

caused by texture weakening and grain refinement. While the pseudo-elastic behavior tended to decrease with RE addition, it largely remained. An additional term was thus introduced to calculate the total strain range, i.e., $\Delta\varepsilon_t = \Delta\varepsilon_e + \Delta\varepsilon_p + \Delta\varepsilon_{an}$, where the total anelastic strain range ($\Delta\varepsilon_{an}$) consisted of both tensile and compressive components. Fatigue crack initiated from the near-surface imperfections, and crack propagation was characterized by fatigue striation-like features.

Keywords: Magnesium alloy; cyclic deformation; anelastic behavior; twinning-detwinning; texture weakening.

1. Introduction

Vehicle lightweighting is today recognized as one of the most important methods to improve fuel efficiency and reduce anthropogenic climate-changing, environment-damaging, costly and human death-causing[1] emissions [1-7] because of the huge environmental concerns and mounting global energy demand in the transportation industry. Indeed, it has recently been portrayed as the storm of lightweighting – a revolution in materials, processes, and business models – which is brewing on the horizon of the automotive industry. Passenger vehicles, usually thought as the less detrimental ones, are in fact reported to be among the most diverse means of transportation due to their abundance [8]. Hence, finding alternatives to reduce the fuel

---

[1] According to Science News entitled "Air pollution kills 7 million people a year" on March 25, 2014 at http://news.sciencemag.org/signal-noise/2014/03/air-pollution-kills-7-million-people-year: "Air pollution isn't just harming Earth; it's hurting us, too. Startling new numbers released by the World Health Organization today reveal that one in eight deaths are a result of exposure to air pollution. The data reveal a strong link between the tiny particles that we breathe into our lungs and the illnesses they can lead to, including stroke, heart attack, lung cancer, and chronic obstructive pulmonary disease."

consumption of passenger vehicles has been of major interest and has been attracting a great deal of research curiosity [4,9]. Actually, fuel efficiency can be ameliorated by about 8% for each 10% weight reduction [10]. In this context ultra-lightweight Mg alloys have attracted considerable interest in the transportation industry because of their low density, high strength-to-weight ratio, and superior damping capacity. Nevertheless, several constraints are faced in the application of magnesium alloys, including high directional anisotropy and poor formability at room temperature. The development of strong texture (i.e., preferred orientation) in the deformation process leads to the tension-compression yield asymmetry and mechanical anisotropy in the wrought magnesium alloys [11,12]. This is related to the hexagonal close-packed (hcp) crystal structure of magnesium and its limited deformation modes [13,14], where mechanical twinning plays a substantial role in the deformation mechanisms. Both the tension-compression yield asymmetry and room-temperature formability could be effectively improved by adding alloying elements, especially rare-earth (RE) elements due to their tendency to induce texture randomization during hot processes (e.g., extrusion or rolling), which leads to the decrease of texture intensities and the activation of basal slip [13-17].

Cyclic deformation and fatigue properties are crucial for the structural applications of magnesium alloys, since the structures and devices undergo dynamic loading in service [14,18-24,]. Consequently, having a clear comprehension of fatigue and cyclic deformation behavior is important in the design and the assessment of durability and safety. Some studies on the fatigue of rare-earth containing magnesium alloys have been reported in the literature [14,18,25-27]. For instance, Yang *et al.* [28] conducted very high cyclic fatigue tests of a RE-containing extruded magnesium alloy Mg-12Gd-3Y-0.5Zr, and observed much relieved tension-compression yield asymmetry and enhanced fatigue failure resistance in comparison with RE-free AZ31 alloy. The fatigue strength of extruded Mg-10Gd-1Nd and Mg-10Gd alloys in the form of S-N curves was also evaluated via stress-controlled high cycle fatigue tests [29]. Limited strain-controlled low cycle fatigue tests on the RE-containing extruded magnesium alloys have been performed as well, including Mg-10Gd-3Y-0.5Zr [14,18,25,26], Mg-3Nd-0.2Zn-0.5Zr [30], Mg-8Gd-3Y-0.5Zr [27,31], where the basal texture was observed to be weakened and the tension-compression yield asymmetry basically disappeared as reflected by the nearly symmetrical hysteresis loops [14,18,25,26]. However, the non-linear or pseudo-elastic behavior still remained, unlike the situation of face-centered cubic (fcc) metals [14,18,25,26,30]. The above RE-containing wrought magnesium alloys with available fatigue data included a relatively large amount of expensive RE elements. Material cost is important in the automotive sector, and needs to be affordable for the general public, thus an Al-free and low (on the order of ~0.2 wt.% Nd) neodymium-containing ZEK100 wrought magnesium sheet alloy has recently been developed.

The microstructure and texture development of ZEK100 alloy have been studied during warm rolling and annealing [16,17]. Forming-limit diagrams were developed at elevated temperatures and varying strain rates, and this alloy reached greater major true fracture strains, by up to 60%, than the AZ31B alloy for all strain paths at all temperatures and strain rates examined [32]. The formability of this alloy in a two-stage forming process with intermediate annealing was also studied [33]. ZEK100 alloy exhibited superior warm formability over AZ31B alloy, indicating the potential for the volume production of magnesium automotive parts [34]. The tensile properties and constitutive behavior of ZEK100 alloy was also studied at varying strain rates and sample orientations at room temperature [35-37]. Although the basal texture was weakened, this alloy still presented anisotropy in the tensile properties and in the bending behavior [36]. While tensile loading-unloading tests with an incremental strain were performed [38], no fatigue data on the ZEK100 magnesium alloy under strain-controlled tests are available in the literature so far. It is unclear if cyclic hardening or softening would occur, to what extent the tension-compression yield asymmetry would remain, and whether pseudo-elastic behavior would still be present, and how it can be quantified. Therefore, the objective of the present study was to identify cyclic deformation behavior of a low RE-containing ZEK100 rolled magnesium alloy in relation to the twinning-detwinning characteristics and non-linear elastic behavior.

2. Material and Experimental Procedure

The test material used in this study was a recently-developed rolled ZEK100 magnesium alloy sheet of 3 mm in thickness, in an annealed condition designated as ZEK100-O supplied by Magnesium Elektron via the University of Waterloo and Magna International Inc. The annealing was done at 500°C for 15 minutes in an electrical oven [32,33]. The chemical composition of the alloy is given in Table 1 [39]. Microstructures were observed using an optical microscope (OM) equipped with an image analysis system, and a scanning electron microscope (SEM) JSM-6380LV along with an Oxford energy dispersive X-ray spectroscopy (EDS) system. Sample preparations were accomplished by following standard metallographic techniques, and microstructural features were revealed using an etchant of acetic picral solution (i.e., 4.2 g picric acid, 10 ml acetic acid, 10 ml H_2O and 70 ml ethanol). Textures were obtained using a PANalytical X-ray diffractometer (XRD) with Cu K_α radiation at 45 kV and 40 mA in a back reflection mode by measuring partial pole figures (i.e., ranging between Ψ=0^o and 75°). Texture data were afterwards analyzed based on MTEX software [40]. It should be noted that the defocusing stemming from the rotation of the XRD sample holder was corrected using the experimental data obtained from magnesium powder diffraction. The same XRD was also used to identify phases in the alloy. The diffraction angle (2θ), at which the X-rays hit the sample, ranged between 20° and 110° with a step size of 0.2° and 10s for each step.

Tensile tests were performed by means of a computerized UNITED tensile testing machine with a sample gauge length of 25 mm (or a parallel length of 32 mm) at a strain rate of 1×10^{-2} s^{-1}. Sub-sized fatigue samples (Fig.1) in accordance with ASTM: E8 standard were machined with the loading axis parallel to the extrusion direction (ED). Strain-controlled “pull-push” fatigue tests were conducted using a computerized INSTRON 8801 fatigue testing system at room temperature (i.e., about 23°C) with a sample gauge length of 12.5 mm (or a parallel length of 16 mm). The test conditions consisted of a zero mean strain (i.e., a strain ratio of R_s=-1 or a completely reversed strain cycle) and a fixed strain rate of 1×10^{-2} s^{-1} with a triangular loading waveform. The low cycle fatigue tests were carried out at varying total strain amplitudes from 0.2% to 1.2%. Two samples were tested at each strain amplitude level. At lower strain amplitudes (e.g., 0.2%, 0.3% and 0.4%), strain-controlled tests were sustained for 10,000 cycles before being converted to load control, with a sine waveform at a frequency of 50 Hz. Once tests were completed, SEM was used to examine the fracture surfaces of fatigued samples, aiming to identify the various features involving fatigue initiation and propagation mechanisms. In addition, a special interest was given to the near fracture surface areas of the fatigued samples, which were cut, mounted, ground, polished and etched to examine the eventual appearance of residual twins.

3. Results and Discussion

3.1 Microstructure

Fig.2 shows a three-dimensional image of the microstructure of the rolled Mg ZEK100 alloy where the three observation directions are indicated (i.e., RD: rolling direction, TD: transverse directions, and ND: normal direction). It is seen that most of the grains in all the surfaces were basically characterized as equiaxed under a quasi-uniform distribution. This was due to the occurrence of dynamic recrystallization (DRX) during rolling which was followed by the annealing treatment [41]. Min and Lin [38] studied the microstructure of ZEK100 Mg alloy sheet in an as-fabricated state, and observed a lot of twins due to the initial cold work in the manufacturing process. After annealing, the pre-existent twins disappeared and equiaxed grains formed, which was in agreement with the results shown in Fig.2. Also, equiaxed grains were observed in other wrought Mg alloys (e.g., extruded AM30 [21,42] and AZ31 [20,22]), which displayed a relatively larger grain size in comparison with the present ZEK100. This was mainly due to the presence of the RE element neodymium (Nd) and the zirconium (Zr), as reported by Mirza *et al.* [18], where an extruded GW103K Mg alloy, containing gadolinium (Gd), yttrium (Y), and zirconium (Zr) elements, exhibited a much smaller grain size due to their resistance to grain growth [43]. A similar effect of Nd on the microstructure of AZ31 magnesium alloy was also reported by Li *et al.* [44]. A typical SEM back-scattered electron image of the rolled ZEK100 sample is shown in Fig.3(a), where some particles were present. EDS line scan revealed that the white particles in Fig.3(a) were Nd- and Zr-containing ones (Fig.3(b)). As pointed out in [18], these RE and Zr-containing particles were capable of resisting the grain growth due to the

Zener pinning (also called the Zener drag effect) [45]. Likewise, other RE-containing particles (e.g., cerium [46] and yttrium [47]) were observed to play a similar role in the refinement of the grains. In addition, in the liquid Mg alloy, the dissolved Zr could effectively limit the growth of nucleating Mg grains via solute segregation while the subsequent constitutional undercooling promoted heterogeneous nucleation events ahead of the solidification front, thus refining the grain as well [48,49].

3.2 X-ray diffraction analysis

Fig.4 shows the XRD pattern of the ZEK100-O Mg alloy. In addition to the obviously dominant α-Mg phase, both Zn and Nd-containing intermetallic compounds were detected in the form of MgZn and $Mg_{12}Nd$ phases, respectively. MgZn and $Mg_{12}Nd$ could also be seen from a typical back-scattered electron SEM image as shown in Fig.5. The EDS point analysis revealed an atom percent of 91.6% Mg and 8.4% Nd for particle A (Fig.5), which had an atomic ratio close to that of $Mg_{12}Nd$. Similarly, an atom percent of 56.2% Mg and 43.8% Zn was obtained for particle B (Fig.5), which was close to the atomic ratio of MgZn. Indeed, the phases of $Mg_{12}Nd$ and MgZn could be seen from the Mg-Nd binary phase diagram [50] and the Mg-Zn binary phase diagram [51,52]. Likewise, Huang *et al.* [53] studied the change and evolution of the intermetallic phases, by increasing the rare-earth Gd content in a ZK60 magnesium alloy, which belonged to the same RE family as the present ZEK100. Their XRD investigations on the extruded ZK60-2.98Gd also revealed the presence of $MgZn_2$ and Mg-Zn-Gd phases. This was related to the much higher Zn (6.27 wt.% Zn) and RE (2.98 wt.% Gd) in their ZK60-2.98Gd alloy, in comparison with the studied ZEK100 (1.3 wt.% Zn and 0.2 wt.% Nd, Table 1). When the amount of Gd was reduced to 0.28 wt.%, the tri-phase Mg-Zn-Gd was no longer present [53]. Thus the absence of a tri-phase in the ZEK100 might be due to the micro-addition of only 0.2 wt.% Nd, which was consumed to form $Mg_{12}Nd$ (Figs 4 and 5). Similarly, Wei *et al.* [54] studied a rare-earth containing cast Mg alloy (Mg-8Zn-1.5MM (misch metal)). They observed that the addition of the 1.5MM had a strong influence on the cast alloy by introducing “interdendritic” phases and structural modification of known binary phases. In particular, a lower weight percent of rare-earth facilitated the formation of the MgZn phase and a considerably high weight percent of rare earth (i.e., 1.5MM in their study) led to the appearance of ternary phases. The presence of the $Mg_{12}Nd$ intermetallic phase in the ZEK100 alloy, as seen from XRD and EDS evaluations (Figs 4 and 5, respectively), would also be associated with the relatively low addition of Nd (0.2 wt.%) in Mg.

Further studies by Grosse *et al.* [55] involved the assessment of the Mg-Nd binary system and presented a series of descriptions about the most favorable circumstances for the appearance of various Mg-Nd phases. A special attention was given to the $Mg_{12}Nd$ phase which was known to be metastable. Similar to Nayeb-Hashemi and Clark [50], Grosse *et al.* [55] qualified $Mg_{12}Nd$ as the richest intermetallic phase in the Mg-Nd system as it was depicted in the Mg-Nd binary phase diagram [52], and pointed out that it could easily be compared with other $Mg_{12}RE$ phases. It should be noted that, although the amount of zirconium (Zr) was slightly higher than that of neodymium (Nd) as listed in Table 1, no Mg-Zr intermetallic phase could be formed which could be understood by observing the Mg-Zr binary phase diagram [56,48].

3.3 Crystallographic texture

Orientation distribution functions (ODF) of the rolled ZEK100 Mg alloy are shown in Fig.6, where the positions of major texture components are indicated (i.e., locations A and B, respectively). It is known that main texture components in the hcp materials can be easily differentiated at a fixed section of φ_2=0° and φ_2=30° [57,58]. As seen from Fig.6, φ_1 direction is along the horizontal axis whereas Φ direction lays in the vertical axis. Based on the Euler angles A (φ_1=0°, Φ=25°, φ_2=30°) and B (φ_1=0°, Φ=25°, φ_2=0°) from Fig.6, two major texture components in this alloy could be identified to be $\mathrm{A}\{0001\}\langle 2\bar{1}\bar{1}0\rangle$ and $\mathrm{B}\{0001\}\langle 10\bar{1}0\rangle$, as illustrated in Fig.7. While the maximum intensity of component A was slightly lower than that of component B, i.e., 3.5 MRD (multiples of random distribution) vs. 3.9 MRD, as seen in Fig.6, the texture intensity was much lower in the ZEK100 alloy than in the RE-free Mg alloys, e.g., 8.5~8.9 MRD in the AM30 alloy [57]. This observation supported the suggestion of texture weakening when RE elements were added in Mg alloys. Likewise, in the texture investigation of ZEK100 Mg alloy, Min and Lin [38] evaluated the (0001) pole figure and reported a maximum intensity of 3.621 MRD which was in good agreement with the obtained results. Another wrought RE-Mg alloy (i.e., Mg-10Gd-3Y-0.5Zr) was studied by Mirza *et al.* [25] who confirmed that the addition of RE elements to Mg alloys had a significant benefit of texture weakening and that even the addition of a small amount of gadolinium (Gd) was susceptible to the reduction of texture intensity in wrought Mg alloys. Hence, a direct analogy could be made with the present Nd-containing alloy with a relatively low MRD value.

3.4 Hysteresis loops and tensile properties

Typical stress-strain hysteresis loops of the first, second and mid-life cycles obtained at a total strain amplitude of 1.2% and a strain ratio of $R_s=-1$ for the ZEK100 alloy are presented in Fig.8, where two additional wrought Mg alloys (i.e., GW103K and AM30 [18,21]) were added for the sake of comparison. The observation of the "opening quarters" of the first-cycle hysteresis loops (Fig.8(a)) could indeed be used to evaluate the yield strength at a strain rate of 1×10^{-2} s^{-1} for each of these alloys. The present ZEK100 alloy had a tensile yield strength of ~225 MPa which lay in-between the two values obtained for the extruded AM30 and GW103K alloys (i.e., ~200 MPa [21] and ~240 MPa [18], respectively). This finding was expected, since the present ZEK100 (with 0.2 wt.% Nd) was compared on purpose with a RE-free Mg alloy (e.g., AM30) and a relatively high RE-containing Mg alloy (GW103K with 10 wt.% Gd and 3 wt.% Y). This comparison once again brought up one of the major benefits from the addition of RE elements to Mg alloys even with moderate amounts, such as the case of the present ZEK100 alloy. Table 2 lists the tensile properties of ZEK100 alloy obtained during tensile tests at a strain rate of 1×10^{-2} s^{-1} at room temperature. An ultimate tensile strength (σ_{UTS}) of 300 MPa was acquired for the rolled ZEK100 alloy, which was fairly close to that of extruded high RE-containing alloys, e.g., GW103K Mg alloy with 10 wt.% Gd and 3 wt.% Y (~318 MPa) [25] and GW123K Mg alloy with 12 wt.% Gd and 3 wt.% Y (~335 MPa) [28]. He *et al.* [59] also reported an equivalent σ_{UTS} value of ~302 MPa for a RE-containing ZK60 alloy (with 1.3 wt.% Gd). It is clear that the slight (0.2 wt.% Nd) addition of Nd in the ZEK100 alloy along with 1.3 wt.% Zn and 0.25 wt.% Zr was pretty effective in improving the tensile properties. In fact, a higher or equivalent elongation of 13.3% (Table 2) was noted for the ZEK100 in comparison with GW103K (8.3% elongation [25]) and AM30 (~13% elongation [21]). The superior ductility of the ZEK100 alloy would be related to its better formability [34].

It is also seen from Fig.8 that the hysteresis loop of the present ZEK100 alloy fell in-between those of the almost symmetrical GW103K and the tilted AM30 especially in the compressive phase. Due to the presence of a high amount of RE elements, GW103K displayed a practically symmetrical hysteresis loop, similar to that in the face-centered cubic (fcc) metals, such as aluminum, nickel and copper, which were controlled by the dislocation slip rather than twinning deformation [60]. The quantification of the hysteresis loops will be given later.

3.5 Cyclic stress and strain responses

The evolution of stress amplitudes and plastic strain amplitudes with respect to the number of cycles at different strain amplitudes from 0.2% to 1.2% is shown in Figs 9 and 10, respectively, under a semi-logarithmic scale along the X axis. It is observed that both stress amplitudes and plastic strain amplitudes augmented, whereas fatigue life of the material diminished with increasing total strain amplitudes. In addition, a slight cyclic softening could be seen at two highest strain amplitudes namely 1.0% and 1.2%, however, almost cyclic stabilization was noted for the remaining strain amplitudes especially at lower values of 0.2%-0.4%. Unlike the present ZEK100, cyclic hardening occurred at higher strain amplitudes due to the occurrence of extensive twinning in the descending and compressive phase and detwinning in the ascending and tensile phase during cyclic deformation along the extrusion direction in the RE-free wrought Mg alloys (e.g., AM30 and AZ31) [19-22,42]. On the other hand, Mirza *et al.* [18] showed that in the case of high RE-containing alloys such as GW103K with about 10 wt.% Gd and 3 wt.% Y, cyclic stabilization was observed up to a strain amplitude of about 1.0% due to the effect of RE elements. The results shown in Figs 9 and 10 helped emphasize the conclusions drawn earlier when interpreting the hysteresis loops (Fig.8), where ZEK100 Mg alloy exhibited, once again, a behavior lying in-between both comparison alloys (e.g., AM30 and GW103K). Similarly, Wu *et al.* [61] studied the cyclic deformation behavior of a RE-rich Mg-10Gd-2.0Y-0.46Zr alloy at 300°C and observed cyclic softening characteristics at different total strain amplitudes, which was in agreement with the results obtained for ZEK100. In addition, the observed cyclic stress responses for ZEK100 could be further corroborated based on the assumptions made by Noster and Scholtes [62] who stated that strain hardening effect was diminutive at room temperature, as they described the effect of temperature on stress responses.

3.6 Fatigue life and strain-life fatigue parameters

Fig.11 displays the total strain amplitude $\Delta\varepsilon_t / 2$ as a function of the number of cycles to failure (i.e., fatigue life) for the rolled ZEK100 Mg alloy, in comparison with the data reported in the literature for both RE-free and RE-containing wrought Mg alloys [15,18,19,21,63]. The run-out data points where no failure occurred at 10^7 cycles or more are labeled by horizontally directing arrows. A relatively enhanced fatigue life was obtained for ZEK100 Mg alloy, when compared to the RE-free alloys (e.g., AM30, AZ31 and AZ61). Besides, when compared with the rest of the RE-containing alloys (e.g., GW103K and ZK60), the current ZEK100 showed the ability of keeping up for a high and equivalent number of cycles to failure at the most total strain amplitudes, although it is an alloy that contained the least RE element (0.2 wt.% Nd, Table 1) among the three alloys. This suggests the effectiveness of Nd addition along with the proper processing or alloy state (annealing O-state), which led to a fairly good strength and ductility (Table 2), since strain-controlled fatigue life is related to both characteristics.

Another way of observing the fatigue behavior was conveniently through the expression of the total strain amplitude consisting of the elastic and plastic strain amplitudes separately, where the elastic strain component was denoted by the Basquin's equation and the plastic strain constituent was known as the Coffin-Manson relation. The equation can be expressed as [19-21,13,64,65],

$$\frac{\Delta\varepsilon_t}{2} = \frac{\Delta\varepsilon_e}{2} + \frac{\Delta\varepsilon_p}{2} = \frac{\sigma'_f\left(2N_f\right)^b}{E} + \varepsilon'_f\left(2N_f\right)^c, \tag{1}$$

where E is the Young's modulus (during fatigue testing, the average value for ZEK100 was ~44.9 GPa), N_f is the number of cycles to failure, σ'_f is the fatigue strength coefficient, b is the fatigue strength exponent, ε'_f is the fatigue ductility coefficient, and c is the fatigue ductility exponent. Fig.12 illustrates the elastic, plastic, and total strain amplitudes as a function of the number of reversals to failure ($2N_f$). In order to make sure that cyclic stabilization, also called cyclic saturation, has already occurred, the stress and strain values of the mid-life cycles were used. Hence, the fatigue life parameters obtained by means of Equ.(1) were presented in Table 3. Begum *et al*. [19] reported a cyclic strain hardening exponent value n' of ~0.34 for a RE-free AZ31 Mg alloy. However, for the present rolled ZEK100 alloy n' was obtained to be ~0.15. The drop in comparison with AZ31 could be explained by the higher yield strength as mentioned earlier and the enhanced cyclic stabilization phenomenon due to the presence of less extensive twinning to be discussed later.

3.7 Cyclic stress-strain curve

Like the monotonic tensile stress-strain curves [66], cyclic stress-strain response is important for determining the properties of fatigue resistance and represents a major aspect in understanding the overall strain-controlled cyclic deformation comportment. It allows to provide a full description of the relationship between the flow stress and plastic strain amplitude under cyclic loading [21,22], which could be expressed as follows,

$$\frac{\Delta\sigma}{2} = K'\left(\frac{\Delta\varepsilon_p}{2}\right)^{n'}, \tag{2}$$

where K' is the cyclic strength coefficient and n' is the cyclic strain hardening exponent [67], with the stress amplitude and plastic strain amplitude both from the mid-life cycles at different total amplitudes applied. Fig.13 illustrates a superposition of the monotonic tensile stress-strain curve at a strain rate of $1\times\ 10^{-2}\ s^{-1}$ and cyclic stress-strain curves (CSSC) [68] at mid-life cycles with the Y-axis stress indicated as the normal stress amplitude ($\frac{\Delta\sigma}{2}$), tensile peak stress, and compressive peak stress (absolute value), respectively, for the ZEK100 Mg alloy tested at a strain ratio of R_s=−1. It is seen that the results obtained from the tensile peak basically matched with those of the monotonic tensile tests, while the results obtained from the compressive peak (absolute value) were positioned below the monotonic stress-strain curve at higher strain amplitudes of 1.0% and 1.2%. This indeed reflected the asymmetry of the mid-life hysteresis loops, as seen in Fig, 8(c). In addition, the monotonic strain hardening exponent n was previously obtained to be about 0.18 (Table 2), whereas the cyclic strain hardening exponent n' was about 0.15 which was slightly lower than n. The fact that the normal CSSC was located below the monotonic stress-strain curve (Fig.13) directly reflected a slight cyclic softening at total strain amplitudes of 1.0% and 1.2%, as seen from Fig.9 and Fig.10. Since the difference between cyclic and monotonic hardening exponents was considered minor (about 0.03) and there was a good overlapping between the monotonic stress-strain curve and CSSC up to total strain amplitude of 0.8 (Fig.13), the cyclic steady comportment was expected. Likewise, Begum *et al.* [19] conducted similar investigations about a RE-free extruded AZ31 Mg alloy and obtained 0.13 and 0.34 for n and n', respectively. Therefore, the authors concluded that the extruded AZ31 was susceptible to be more hardened under cyclic loading conditions rather than the monotonic ones.

3.8 Fractography

Fig.14(a) and (b) display an overall view of fatigued samples tested at total strain amplitudes of 0.4% and 1.0%, respectively. It is seen that fatigue cracks initiated from the specimen surface. As seen from the images taken at a slightly higher magnifications (Fig.14(c) and (d)), crack initiation occurred from the specimen surface or near surface defects. It was clear that fatigue crack propagation area was larger at a lower strain amplitude of 0.4% than at a higher strain amplitude of 1.0% (Fig.14(a) and (b)). The SEM images taken at a higher magnification in the crack propagation area (Fig.15(a) and (b)) showed that at both strain amplitudes, the fatigue crack propagation region encompassed some striation-like features which were basically the distinct line markings appearing on the fractured surface. Similar characteristics were presented in [19-22,61,69] as well. These striation-like markings were noted to be perpendicular to the crack propagation direction. In addition, a few secondary cracks could be perceived in the crack propagation region (Fig.15(a)). In Fig.15(b), some shallow dimples along with tear ridges marked by arrows were visible, indicating the presence of larger plastic deformation in front of the crack tip at the higher strain amplitude.

3.9 Qualification of hysteresis loop asymmetry and skewness characteristics

Since the present ZEK100 alloy exhibited a certain extent of asymmetrical stress-strain behavior in tension and compression (Fig.8 and Fig.13), which are of major concern in relation to the influence of RE element addition as well as the twinning-detwinning behavior, it is thus necessary to quantify the asymmetry and skewness based on the stress-strain hysteresis loops. In this context, an eccentricity parameter e is first defined, which is simply the horizontal “gap” in the form of strain amount by which the point of intersection of a line passing through the upper and lower peaks of the loop with the X-axis is shifted from the coordinate origin, as shown in Fig.16 for the stress-strain hysteresis loops of mid-life cycles at a total strain amplitude of 1.2% and a strain ratio of R_s=−1. The eccentricity values for ZEK100, AM30 and GW103K alloys are indicated to be e_Z, e_A, and e_G, respectively. It should be noted that the eccentricity could also be observed vertically, however it was only accounted for horizontally to avoid repetitive information. A perfectly symmetrical hysteresis loop, such as the case of face-centered cubic (fcc) metals (e.g., aluminum, nickel and copper) [60,70], would have a zero eccentricity value. Because of the skewness of its shape and its high asymmetry, the extruded AM30 had a value of e_A = ~0.25%. However, the nearly symmetric GW103K, which exhibited a characteristic closer to the fcc materials as mentioned earlier, admitted a value of e_G = ~0.02%, meaning that the loop was negligibly shifted from the origin. As expected, a value of e_Z = 0.1% was obtained for the present ZEK100, which fell in-between e_A and e_G. These eccentricity values are summarized in

Table 4. Thus, this parameter helps quantify the asymmetry of the stress-strain hysteresis loops, which is directly linked to the amelioration of the fatigue behavior of the Mg alloys by the addition of the RE elements.

Fig.17 illustrates two parameters which are the angle deviation $\Delta\alpha$ and the relative slope change d. For instance, Fig.17(b) displays these two parameters for the ZEK100 Mg alloy, where two separate lines (L_1 and L_2) were generated, with L_1 plotted from the lower peak B passing through the origin as a reference line, and L_2 plotted from the lower peak to upper peak points of the hysteresis loop (points A and B in Fig.17(b)). Let us set α_3 to be the angle between L_1 and the horizontal axis and α_4 to be the angle between L_2 and the horizontal axis, then $\Delta\alpha_Z$ for the ZEK100 alloy becomes,

$$\Delta\alpha_Z = \alpha_4 - \alpha_3. \tag{3}$$

The relative slope change is also introduced through the example of ZEK100 alloy in Fig.17(b), which is computed as follows,

$$d_Z = \left| \frac{S_{Z2} - S_{Z1}}{S_{Z1}} \right| \times 100, \tag{4}$$

where S_{Z1} and S_{Z2} are the slopes of lines L_1 and L_2, respectively. For the sake of comparison, the above defined parameters were also determined for AM30 and GW103K alloys, as shown in Fig.17(a) and (c), respectively. The obtained values were summarized in Table 4. It is clear that the extruded AM30 Mg alloy exhibited the highest values of both the relative slope change and the angle deviation (d_A = 34.5% and $\Delta\alpha_A$ = 11.5°, respectively), stemming from the strong asymmetry and the distorted shape of its cyclic hysteresis loop, whereas the extruded GW103K Mg alloy presented the lowest values (d_G = 4.6% and $\Delta\alpha_G$ = 1.0°), which reflected the closeness of the hysteresis loop of this high RE-containing alloy to that of a fcc alloy, due to the addition of the 10 wt.% Gd and 3 wt.% Y [18,25]. As expected, the results for ZEK100 fell in-between the two comparison alloys (i.e., d_Z = 15.8% and $\Delta\alpha_Z$ = 5.1°), which once again revealed that the presence of 0.2 wt.% Nd is a major factor in ameliorating its cyclic deformation features compared with the RE-free alloys (e.g., extruded AM30).

The fourth parameter proposed in this study is to quantify the non-linear anelastic behavior in tension and compression, separately, so as to achieve the total anelastic strain. In the best case scenario concerning the symmetrical hysteresis loops, such as the case of fcc alloys, the total strain range ($\Delta\varepsilon_t$) from a hysteresis loop would simply consist of [64],

$$\Delta\varepsilon_t = \Delta\varepsilon_e + \Delta\varepsilon_p , \tag{5}$$

where $\Delta\varepsilon_e$ is the total elastic strain range and $\Delta\varepsilon_p$ is the total plastic strain range. When the hysteresis loop exhibits a symmetrical shape, the total elastic strain range could be expressed as,

$$\Delta\varepsilon_e = \Delta\varepsilon_{e-t} + \Delta\varepsilon_{e-c} , \tag{6}$$

where $\Delta\varepsilon_{e\text{-}t}$ is the tensile elastic strain range and $\Delta\varepsilon_{e\text{-}c}$ is the compression elastic strain range. However, in the presence of tension-compression asymmetry in wrought magnesium alloys, Equs (5) and (6) are no longer valid, since no non-linear or pseudo-elastic behavior is taken into account. An additional term, representing the total anelastic strain range ($\Delta\varepsilon_{an}$) is necessary, which can be written as two components,

$$\Delta\varepsilon_{an} = \Delta\varepsilon_{an-t} + \Delta\varepsilon_{an-c} , \tag{7}$$

where $\Delta\varepsilon_{an\text{-}t}$ is the tensile anelastic strain range and $\Delta\varepsilon_{an\text{-}c}$ is the compressive anelastic strain range which are indicated in Fig.18 in the case of ZEK100 alloy. Then, the total strain range becomes,

$$\Delta\varepsilon_t = \Delta\varepsilon_e + \Delta\varepsilon_p + \Delta\varepsilon_{an} . \tag{8}$$

The obtained values of tensile, compressive and total anelastic strain ranges for ZEK100 and two associated alloys AM30 and GW103K are summarized in Table 4. As anticipated, AM30 exhibited the highest values for the anelastic parameters, followed by ZEK100, and then GW103K, which displayed less noticeable pseudo-elastic comportment due to a high content of RE elements.

3.10 Twinning-detwinning behavior

Twinning in the plastic deformation of Mg alloys is important [18,71,80]. In the processing (e.g., extrusion, rolling), wrought magnesium alloys are deformed in such a way that the majority of grains have their basal planes approximately parallel to the process direction [13,72]. Therefore, if a load is applied along this direction, the activation stress would be comparatively low for the deformation twinning in compression (i.e., extension twinning) or in tension (i.e., basal slip and/or de-twinning) [18]. The activation stress would be fairly high in the case of prismatic and pyramidal slip systems for Mg alloys at room temperature [73]. Consequently, twinning and de-twinning interchange by alternating activities at the time of cyclic loading. Wu *et al.* [74] stated in this context that most of the twins formed during compression vanished when the load was overturned. During cyclic deformation residual twins got progressively cumulated with increasing number of cycles [42,75]. Fig.19 displays the optical micrographs of the areas near the fracture surface at a strain amplitude of 1.2%, showing the overall distribution of residual twins in a ZEK100 fatigued sample. Similarly, Mirza *et al.* [18] and Fan *et al.* [42] reported dense residual twins near the fatigue fracture surface of the extruded AM30. They pointed out that the occurrence of these twins was related to the inadequate number of slip systems at room temperature. In fact, Brown *et al.* [76] reported that twinning was the only deformation mode which happened to be activated and which had the ability of providing *c*-axis straining at room temperature. This is associated with the low crystal symmetry of hcp structures, in addition to the previously discussed strong preferred orientations for wrought magnesium alloys.

Fig.19(b) demonstrates that many twins were indeed present in the microstructure. Hence, twinning was among the governing deformation mechanisms in the ZEK100 Mg alloy. In contrast, in Fig.19(c) a lesser extent of twinning was observed, which basically occurred in some large grains. This implicates that in some regions basal slip was a dominant mechanism, thus leading to the better symmetry of hysteresis loops of the ZEK100 Mg alloy in comparison with, for instance, AM30 alloy (Fig.8). In fact, twinning deformation was highly implicated in causing the asymmetry of wrought Mg alloys, which was generally characterized by an important tension-compression asymmetry as demonstrated by Wu *et al*. [74]. This asymmetry was mainly accredited to the extensive $\{10\bar{1}2\}\langle10\bar{1}1\rangle$ extension twinning under compressive deformation along the process direction [13,77,78]. Gharghouri *et al.* [79] also noted that the pseudo-elastic effect in pure Mg specimens may be originated from the fact that $\{10\bar{1}2\}$ extension twins grow and shrink with the increase and decrease of the applied load, leading finally to the presence of residual twins shown in Fig.19 for the ZEK100 fatigued samples.

4. Conclusions

The strain-controlled low cycle fatigue properties and pseudo-elastic behavior of a low (0.2 wt.%) rare-earth element Nd-containing wrought ZEK100 magnesium alloy in an annealed state were studied. The following conclusions can be drawn from this investigation:

1) The microstructure of the ZEK100 alloy in the annealing state consisted of equiaxed grains due to the occurrence of dynamic recrystallization. The alloy also contained some $Mg_{12}Nd$ and MgZn particles. The addition of 0.2 wt.% Nd along with 1.3 wt.% Zn and 0.25 wt.% Zr in the alloy led to the weakening of basal texture in comparison with the extruded RE-free AZ31 and AM30 alloys.

2) While slight cyclic softening was observed at high strain amplitudes of 1.0% and 1.2%, cyclic stabilization basically occurred at lower strain amplitudes. The fatigue life of the ZEK100 alloy determined via the strain-controlled fatigue tests was longer than that of the extruded RE-free Mg alloys, as a result of a fairly good combination of strength with ductility in this alloy.

3) Although the stress-strain hysteresis loops of the ZEK100 alloy were not so symmetrical as those of the high (~10 wt.%) RE-containing Mg alloys, the extent of asymmetry and skewness of the loops was effectively improved in comparison with the extruded RE-free AZ31 and AM30 alloys. This indicated that the small addition of 0.2 wt.% Nd in the ZEK100 alloy played a significant role in overpowering the incidence of excessive twinning via texture weakening and grain refinement.

4) While the anelastic (or non-linear or pseudo-elastic) behavior exhibited a decreasing trend with the addition of RE elements in Mg alloys, it still largely remained, which was accounted as an additional term in calculating the total strain range, i.e., $\Delta\varepsilon_t = \Delta\varepsilon_e + \Delta\varepsilon_p + \Delta\varepsilon_{an}$. The

total anelastic strain range ($\Delta\varepsilon_{an}$) further consisted of two components of tensile and compressive anelastic strain ranges.

5) Three parameters (i.e., eccentricity, the angle deviation, and the relative slope change) were introduced to quantify the asymmetry and skewness of the hysteresis loops. The results evaluated for the current ZEK100 alloy lay always in-between those for the RE-free Mg alloys and high RE-containing Mg alloys.

6) Fatigue crack initiation was observed to occur from the specimen surface or near-surface imperfections. Crack propagation region encompassed fatigue striation-like features, which were normal to the crack propagation direction.

Acknowledgements

The authors would like to thank the Natural Sciences and Engineering Research Council of Canada (NSERC) and AUTO21 Network of Centers of Excellence for providing financial support. The authors would like to thank Dr. T. Skszek and Dr. X.P. Niu (Magna International Inc.) and Professor M. Worswick (University of Waterloo) for supplying test materials, and Dr. R. Tandon and Dr. B. Davies (Magnesium Elektron) for supplying magnesium powders for the defocusing calibration. One of the authors (D.L. Chen) is also grateful for the financial support by the Premier's Research Excellence Award (PREA), NSERC-Discovery Accelerator Supplement (DAS) Award, Automotive Partnership Canada (APC), Canada Foundation for Innovation (CFI), and Ryerson Research Chair (RRC) program. The authors would also like to thank Messrs. A. Machin, Q. Li, C. Ma, J. Amankrah and R. Churaman for easy access to the laboratory facilities of Ryerson University and their assistance in the experiments.

References

[1] Barrett S, Lenton TM, Millner A, Tavoni A, Carpenter S, Anderies JM, Chapin FS, Crepin AS, Daily G, Ehrlich P, Folke C., Galaz V, Hughes T, Kautsky N, Lambin EF, Naylor N, Nyborg K, Polasky S, Scheffer M, Wilen J, Xepapadeas A, Zeeuw AD. Climate engineering reconsidered. Nature Climate Change 2014; 4:527-529.

[2] Titley D. Ghosts from the past. Science 2014;345:361.

[3] McNutt M. Climate change impacts. Science 2013;341:435.

[4] Schaedler TA, Jacobsen AJ, Carter WB. Toward lighter, stiffer materials. Science 2013;341: 1181-1182.

[5] Pollock TM. Weight loss with magnesium alloys. Science 2010;328:986-987.

[6] Nie JF, Zhu YM, Liu JZ, Fang XY. Periodic segregation of solute atoms in fully coherent twin boundaries. Science 2013;340:957-960.

[7] Murray J, King D. Oil's tipping point has passed. Nature 2012;481:433-435.

[8] Anderson M, Auffhammer M. Pounds that kill: the external costs of vehicle weight. Rev Econ Stud 2014;81: 535-571.

[9] Chow E, Heywood J, Speth R. Benefits of a higher octane standard gasoline for the US light-duty vehicle fleet. SAE Tech Paper 2014;1.

[10] Joost WJ. Reducing vehicle weight and improving US energy efficiency using integrated computational materials engineering. J Min Met Mat S 2012;64:1032-1038.

[11] Stanford N, Atwell D, Barnett MR. The effect of Gd on the recrystallization, texture and deformation behaviour of magnesium-based alloys. Acta Mater 2010;58:6773-6783.

[12] Lin XZ, Chen DL. Strain hardening and strain-rate sensitivity of an extruded magnesium alloy. J Mater Eng Perform 2008;17:894-901.

[13] Mirza FA, Chen DL. In: Zhang S, Zhao DL, editors. Fatigue of magnesium alloys (Chapter 13). Aerospace Materials Handbook 2013. New York: CRC Press, Taylor & Francis:647-698.

[14] Mirza FA, Chen DL. Fatigue of rare-earth containing magnesium alloys: A review. Fatigue Fract Eng M 2014;37:831-853.

[15] Jordon JB, Gibson JB, Horstmeyer MF, Kadiri HE, Luo AA. Effect of twinning, slip, and inclusions on the fatigue anisotropy of extrusion-textured AZ61 magnesium alloy. Mater Sci Eng A 2011;528:6860-6871.

[16] Kainer KU, Wendt J, Hantzsche K, Bohlen J, Yi SB, Letzig D. Development of the microstructure and texture of RE containing magnesium alloys during hot rolling. Mater Sci Forum 2010;654:580-585.

[17] Samman TA, Li X. Sheet texture modification in magnesium-based alloys by selective rare earth alloying. Mater Sci Eng A 2011;528:3809-3822.

[18] Mirza FA, Chen DL, Li DJ, Zeng XQ. Low cycle fatigue of a rare-earth containing extruded magnesium alloy. Mater Sci Eng A 2013;575:65-73.

[19] Begum S, Chen DL, Xu S, Luo AA. Low cycle fatigue properties of an extruded AZ31 magnesium alloy. Int J Fatigue 2009;31.4:726-735.

[20] Lin XZ, Chen DL. Strain controlled cyclic deformation behavior of an extruded magnesium alloy. Mater Sci Eng A 2008;496:106-113.

[21] Begum S, Chen DL, Xu S, Luo AA. Strain-controlled low-cycle fatigue properties of a newly developed extruded magnesium alloy. Metall Materials Trans A 2008;39:3014-3026.

[22] Begum S, Chen DL, Xu S, Luo AA. Effect of strain ratio and strain rate on low cycle fatigue behavior of AZ31 wrought magnesium alloy. Mater Sci Eng A 2009;517:334-343.

[23] Ogarevic VV, Stephens RI. Fatigue of magnesium alloys. Annu Rev Mater Sci 1990;20: 141-177.

[24] Potzies C, Kainer KU. Fatigue of magnesium alloys. Adv Eng Mater 2004;6:281-289.

[25] Mirza FA, Chen DL, Li DJ, Zeng XQ. Effect of strain ratio on cyclic deformation behavior of a rare-earth containing extruded magnesium alloy. Mater Sci Eng A 2013;588:250-259.

[26] Mirza FA, Chen DL, Li DJ, Zeng XQ. Cyclic deformation of rare-earth containing magnesium alloys. Adv Mater Res 2014;891:391-396.

[27] Wang FH, Dong J, Jiang YY, Ding WJ. Cyclic deformation and fatigue of extruded Mg-Gd-Y magnesium alloy. Mater Sci Eng A 2013; 561:403-410.

[28] Yang F, Lv F, Yang XM, Li SX, Zhang ZF, Wang QD. Enhanced very high cycle fatigue performance of extruded Mg–12Gd–3Y–0.5 Zr magnesium alloy. Mater Sci Eng A 2011;528:2231-2238.

[29] Maier P, Tober G, Mendis CL, Müller S, Hort N. Influence of Nd in extruded Mg-10Gd base alloys on fatigue strength. Adv Mater Res 2014;783:419-424.

[30] Mirza FA, Chen DL, Li DJ, Zeng XQ. Low cycle fatigue of an extruded Mg-3Nd-0.2Zn-0.5Zr magnesium alloy. Mater Des 2014;64:63-73.

[31] Wang FH, Dong J, Feng ML, Sun J, Ding WJ, Jiang YY. A study of fatigue damage development in extruded Mg-Gd-Y magnesium alloy. Mater Sci Eng A 2014;589:209-216.

[32] Antoniswamy AR, Carpenter AJ, Carter JT, Hector Jr LG, Taleff EM. Forming-Limit Diagrams for Magnesium AZ31B and ZEK100 Alloy Sheets at Elevated Temperatures. J Mater Eng Perform 2013;22:3389-3397.

[33] Min J, Lin J, Li J. Forming limits of Mg alloy ZEK100 sheet in preform annealing process. Mater Des 2014;53:947-953.

[34] Niu XP, Skszek T, Fabischek M, Zak A. Low temperature warm forming of magnesium ZEK100 sheets for automotive applications. Adv Mater Res 2014;783:431-436.

[35] Kurukuri S, Worswick M, Bardelcik A, Mishra R, Carter J. Constitutive behavior of commercial grade ZEK100 magnesium alloy sheet over a wide range of strain rates. Metall Mater Trans A 2014;45:3321-3337.

[36] Aslam I, Li B, McClelland Z, Horstemeyer SJ, Ma Q, Wang PT, Horstemeyer MF. Three-point bending behavior of a ZEK100 Mg alloy at room temperature. Mater Sci Eng A 2014;590:168-173.

[37] Martin G, Sinclair CW, Lebensohn R. Microscale plastic strain heterogeneity in slip dominated deformation of magnesium alloy containing rare earth. Mater Sci Eng A 2014;603:37-51.

[38] Min JY, Lin JP. Anelastic behavior and phenomenological modeling of Mg ZEK100-O alloy sheet under cyclic tensile loading-unloading. Mater Sci Eng A 2013;561:174-182.

[39] Kurukuri S, Bardelcik A, Worswick MJ, Mishra RQ, Carter JT. High strain rate characterization of ZEK100 magnesium rolled alloy sheet. EPJ Web Conf, EDP Sciences 2012;26.

[40] Bachmann F, Hielscher FR, Schaeben H. Texture analysis with MTEX free and open source software toolbox. Solid State Phenom 2010;160:63-68.

[41] He YB, Pan QL, Chen Q, Zhang ZY, Liu XY, Li WB. Modeling of strain hardening and dynamic recrystallization of ZK60 magnesium alloy during hot deformation. T Nonferr Metal SOC 2012;22:246-254.

[42] Fan CL, Chen DL, Luo AA. Dependence of the distribution of deformation twins on strain amplitudes in an extruded magnesium alloy after cyclic deformation. Mater Sci Eng A 2009;519:38-45.

[43] Li WP, Zhou H, Li ZF. Effect of gadolinium on microstructure and rolling capability of AZ31 alloy. J Alloy Compd 2009;475:227-232.

[44] Li MZ, Wang YQ, Li C, Liu XG, Xu BS. Effects of neodymium rich rare earth elements on microstructure and mechanical properties of as cast AZ31 magnesium alloy. Mater Sci Tech 2011;27:1138-1142.

[45] Nes E, Ryum N, Hunderi O. On the Zener drag. Acta Metall 1985;33:11-22.

[46] Liu SF, Li B, Wang XH, Su W, Han H. Refinement effect of cerium, calcium and strontium in AZ91 magnesium alloy. J Mater Proc Tech 2009;209:3999-4004.

[47] Luo ZA, Xie GM, Ma ZY, Wang GL, Wang GD. Effect of yttrium addition on microstructural characteristics and superplastic behavior of friction stir processed ZK60 alloy. J Mater Sci Tech 2013;29:1116-1122.

[48] Arroyave R, Shin D, Liu ZK. Modification of the thermodynamic model for the Mg-Zr system. CALPHAD 2005;29:230-238.

[49] Lee YC, Dahle AK, St. John DH. The role of solute in grain refinement of magnesium. Metall Mater Trans A 2000;31:2895-2906.

[50] Hashemi AAN, Clark JB. The Mg-Nd system (Magnesium-Neodymium). J Phase Equilib 1988;9:618-623.

[51] Okamoto H. Comment on Mg-Zn (magnesium-zinc). J Phase Equilib 1994;15:129-130.

[52] Hashemi AAN. Phase diagrams of binary magnesium alloys. ASM Inter 1988, Metals Park, Ohio 44073;370.

[53] Huang ZH, Qi WJ, Xu J. Effects of Gd on microstructure and mechanical property of ZK60 magnesium alloy. T Nonferr Metal SOC 2013;23:2568-2576.

[54] Wei LY, Dunlop GL, Westengen H. The intergranular microstructure of cast Mg-Zn and Mg-Zn-rare earth alloys. Metall Mater Trans A 1995;26:1947-1955.

[55] Gorsse S, Hutchinson CR, Chevallier B, Nie JF. A thermodynamic assessment of the Mg–Nd binary system using random solution and associate models for the liquid phase. J Alloy Compd 2005;392:253-262.

[56] Okamoto H. Mg-Zr (Magnesium-Zirconium). J Phase Equilib Diff 2007;28.3:305-306.

[57] Sarker D, Chen DL. Texture transformation in an extruded magnesium alloy under pressure. Mater Sci Eng A 2013;582:63-67.

[58] Biswas S, Beausir B, Toth LS, Suwas S. Evolution of texture and microstructure during hot torsion of a magnesium alloy. Acta Mater 2013;61:5263-5277.

[59] He SM, Peng LM, Zeng XQ, Ding WJ, Zhu YP. Comparison of the microstructure and mechanical properties of a ZK60 alloy with and without 1.3 wt.% gadolinium addition. Mater Sci Eng A 2006;433:175-181.

[60] Zhu YT, Wu XL, Liao XZ, Narayan J, Kecskes LJ, S.N Mathaudhu SN. Dislocation–twin interactions in nanocrystalline fcc metals. Acta Mater 2011;59:812-821.

[61] Wu L, Yang Z, Xia W, Chen Z, Yang L. The cyclic softening and evolution of microstructures for Mg–10Gd–2.0 Y–0.46 Zr alloy under low cycle fatigue at 573K. Mater Des 2012;36:47-53.

[62] Noster U, Scholtes B. Isothermal strain-controlled quasi-static and cyclic deformation behavior of magnesium wrought alloy AZ31. Z Metall Kd 2003;94:559-563.

[63] Yin SW, Wang CH, Diao YD, Wu SD, Li SX. Influence of grain size and texture on the yield asymmetry of Mg-3Al-1Zn alloy. J Mater Sci Tech 2011;27:29-34.

[64] Dieter GE, Mechanical Metallurgy, SI metric ed. New York: McGraw-Hill Inc.;1986

[65] Patel HA, Chen DL, Bhole SD, Sadayappan K. Cyclic deformation and twinning in a semi-solid processed AZ91D magnesium alloy. Mater Sci Eng A 2010;528:208-219.

[66] Ma Z, Zhao H, Hu X, Cheng H, Lu S, Zhang L. Influences of tensile pre-strain and bending pre-deflection on bending and tensile behaviors of an extruded AZ31B magnesium alloy. Mater Des 2014;64:566-572.

[67] Antunes RA, Lopes de Oliveira MC. Materials selection for hot stamped automotive body parts: An application of the Ashby approach based on the strain hardening exponent and stacking fault energy of materials. Mater Des 2014;63:247-256.

[68] Sundaraman S G, Radhakrishnan VM. On cyclic stress-strain behaviour and low cycle fatigue life. Mater Des 2002;23:249-254.

[69] Canadija M, Guo X, Lanc D, Yang W, Brnic J. Low cycle fatigue and mechanical properties of magnesium alloy Mg-6Zn-1Y-0.6Ce-0.6Zr at different temperatures. Mater Des 2014;59:287-295.

[70] Zhou N, Zhang Z, Jin L, Dong J, Chen B, Ding W. Ductility improvement by twinning and twin-slip interaction in a Mg-Y alloy. Mater Des 2014;56:966-974.

[71] Sarker D, Chen DL. Detwinning and strain hardening of an extruded magnesium alloy during compression. Scripta Mater 2012;67:165-168.

[72] Agnew SR, Mehrotra P, Lillo TM, Stoica GM, Liaw PK. Crystallographic texture evolution of three wrought magnesium alloys during equal channel angular extrusion. Mater Sci Eng A 2005;408:72-78.

[73] Barnett MR. A Taylor model based description of the proof stress of magnesium AZ31 during hot working. Metall Mater Transa A 2003;34:1799-1806.

[74] Wu L, Jain A, Brown DW, Stoica GM, Agnew SR, Clausen B, Fielden D, Liaw PK. Twinning–detwinning behavior during the strain-controlled low-cycle fatigue testing of a wrought magnesium alloy, ZK60A. Acta Mater 2008;56:688-695.

[75] Bohlen J, Nurnberg MR, Senn JW, Letzig D, Agnew SR. The texture and anisotropy of magnesium–zinc–rare earth alloy sheets. Acta Mater 2007;55:2101-2112.

[76] Brown DW, Agnew SR, Bourke MAM, Holden TM, Vogel SC, Tome CN. Internal strain and texture evolution during deformation twinning in magnesium. Mater Sci Eng A 2005;399:1-12.

[77] Avedesian MM, Baker H. Magnesium and magnesium alloys. ASM inter 1999.

[78] Sheldon RC. Magnesium and its alloys. John Wiley & Sons, New York 1960.

[79] Gharghouri MA, Weatherly GC, Embury JD, Root J. Study of the mechanical properties of Mg-7.7 at.% Al by in-situ neutron diffraction. Philos Mag A 1999;79:1671-1695.

[80] Wang L, Huang G, Quan Q, Bassani P, Mostaed E, Vedani M, Pan F. The effect of twinning and detwinning on the mechanical property of AZ31 extruded magnesium alloy during strain path changes. Mater Des 2014;63:177:184.

Table captions

Table 1 Chemical composition of ZEK100 Mg alloy sheet (wt.%).

Table 2 Tensile properties of ZEK100 alloy obtained at a strain rate of 1×10^{-2} s^{-1} at room temperature.

Table 3 Low cycle fatigue parameters obtained for the rolled ZEK100 Mg alloy.

Table 4 Parameters proposed to describe the non-linear characteristics in Mg alloys.

Figure captions

Fig.1 Fatigue test specimen geometry and dimensions (in mm) for the ZEK100 Mg alloy.

Fig.2 Three-dimensional image of the microstructure of the rolled ZEK100 Mg alloy, where RD stands for the rolling direction, TD denotes the transverse directions, and ND indicates the normal direction.

Fig.3 (a) A typical SEM back-scattered electron image, and (b) EDS line scan results across a position indicated by the dashed line in (a).

Fig.4 X-ray diffraction pattern of the ZEK100 Mg alloy.

Fig.5 SEM back-scattered electron image specifying EDS point analysis locations and the corresponding composition at particles A and B, respectively.

Fig.6 ODF sections at φ_2=0° and φ_2=30° of the ZEK100 Mg alloy.

Fig.7 Main texture components A and B identified from the Euler angles.

Fig.8 Characteristic stress-strain hysteresis loops of the (a) first cycle, (b) second cycle, and (c) mid-life cycle at a total strain amplitude of 1.2% and strain ratio $R_s=-1$ for the rolled ZEK100 alloy, in comparison with the extruded AM30 and GW103K alloys [18,21].

Fig.9 Stress amplitude vs. the number of cycles at different total strain amplitudes.

Fig.10 Plastic strain amplitude vs. the number of cycles at different total strain amplitudes.

Fig.11 Total strain amplitude as a function of the number of cycles to failure for the rolled ZEK100 Mg alloy, in comparison with the data reported in the literature for various wrought Mg alloys.

Fig.12 Evaluation of strain-life fatigue parameters in the form of log-elastic, plastic and total strain amplitudes vs. log-number of reversals to failure, respectively.

Fig.13 Cyclic stress-strain curves (CSSC) at mid-life cycles at a strain ratio of $R_s=-1$ in the ZEK100 Mg alloy.

Fig.14 SEM micrographs of overall fracture surfaces of the specimens fatigued at a strain amplitude of (a) 0.4% and (b) 1.0%, respectively, and near crack initiation area at (c) 0.4% and (d) 1.0% as well.

Fig.15 SEM micrographs of the fatigue crack propagation area in the specimens fatigued at a strain amplitude of (a) 0.4% and (b) 1.0%, respectively.

Fig.16 Stress-strain hysteresis loops of mid-life cycles at a total strain amplitude of 1.2% and a strain ratio $R_s=-1$ for the rolled ZEK100, extruded AM30 and GW103K alloys, respectively, showing the definition of eccentricity values of these alloys along the strain axis.

Fig.17 Stress-strain hysteresis loops of mid-life cycles at a total strain amplitude of 1.2% and strain ratio of $R_s=-1$ for (a) extruded AM30, (b) rolled ZEK100, and (c) GW103K alloys, respectively, showing the parameters of slope change and angle deviation.

Fig.18 Stress-strain hysteresis loop of mid-life cycle at a total strain amplitude of 1.2% and strain ratio of $R_s=-1$ for the rolled ZEK100 Mg alloy, illustrating the anelastic behavior in tension and compression separately.

Fig.19 (a) Optical micrographs of the areas near the fracture surface, showing the overall distribution of residual twins in a sample of ZEK100 alloy fatigued at a strain amplitude of 1.2% with emphasis on two regions (b) and (c), respectively.

Table 1 Chemical composition of ZEK100 Mg alloy sheet (wt.%).

Base material	**Zn**	**Zr**	**Nd**	**Mn**	**Mg**
ZEK100	1.3	0.25	0.2	0.01	Bal.

Table 2 Tensile properties of ZEK100 alloy obtained at a strain rate of 1×10^{-2} s^{-1} at room temperature.

	σ_{YS}, MPa	**σ_{UTS}, MPa**	**Elongation, %**	**n**	**$\sigma_{UTS} / \sigma_{YS}$**
ZEK100	225	300	13.3	0.18	1.33

Table 3 Low cycle fatigue parameters obtained for the rolled ZEK100 Mg alloy.

Low cycle fatigue parameters	**ZEK100**
Cyclic strain hardening exponent, n'	0.15
Cyclic strength coefficient, K', MPa	542
Fatigue strength coefficient, σ'_f, MPa	654
Fatigue strength exponent, b	-0.14
Fatigue ductility coefficient, ε'_f	0.18
Fatigue ductility exponent, c	-0.68

Table 4 Parameters proposed to describe the non-linear characteristics in Mg alloys.

	AM30	**ZEK100**	**GW103K**
Eccentricity along the strain axis (e), %	$e_A = 0.25$	$e_Z = 0.1$	$e_G = 0.02$
Relative slope change (d), %	$d_A = 34.5$	$d_Z = 15.8$	$d_G = 4.6$
Angle deviation ($\Delta\alpha$), degrees	$\Delta\alpha_A = 11.5°$	$\Delta\alpha_Z = 5.1°$	$\Delta\alpha_G = 1.0°$

Tensile anelastic strain range ($\Delta\varepsilon_{an-t}$), %	0.055	0.045	0.025
Compressive anelastic strain range ($\Delta\varepsilon_{an-c}$), %	0.11	0.08	0.075
Total anelastic strain range ($\Delta\varepsilon_{an}$), %	0.165	0.125	0.1

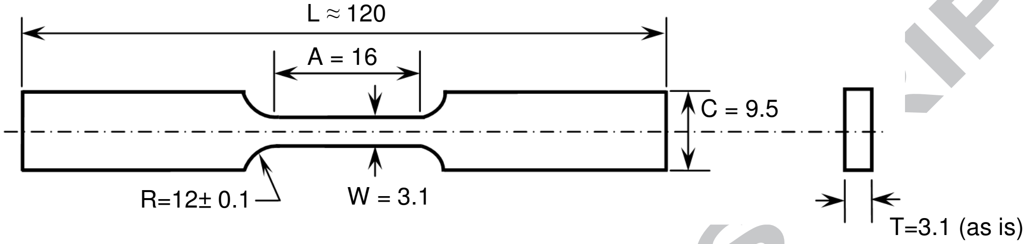

Fig.1 Fatigue test specimen geometry and dimensions (in mm) for the ZEK100 Mg alloy.

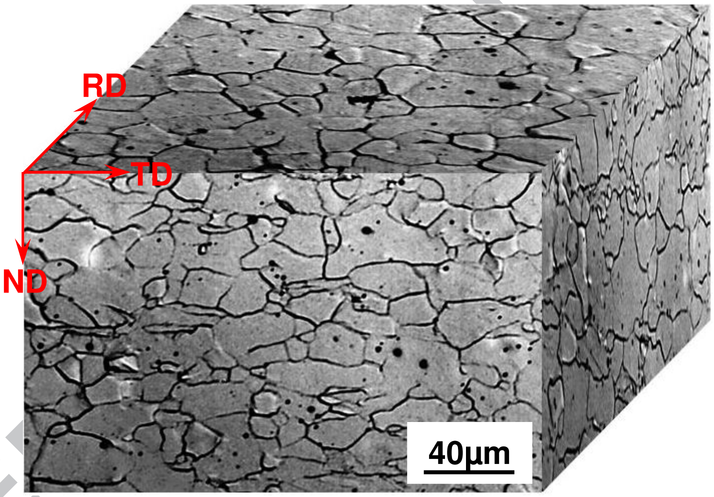

Fig.2 Three-dimensional image of the microstructure of the rolled ZEK100 Mg alloy, where RD stands for the rolling direction, TD denotes the transverse directions, and ND indicates the normal direction.

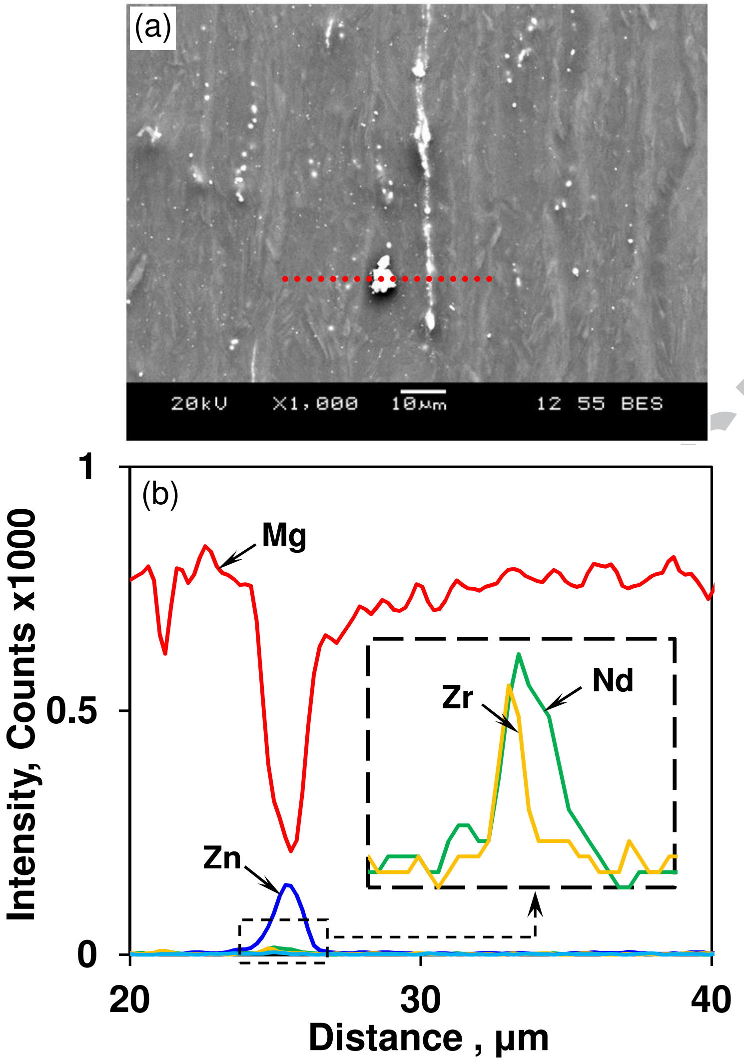

Fig.3 (a) A typical SEM back-scattered electron image, and (b) EDS line scan results across a position indicated by the dashed line in (a).

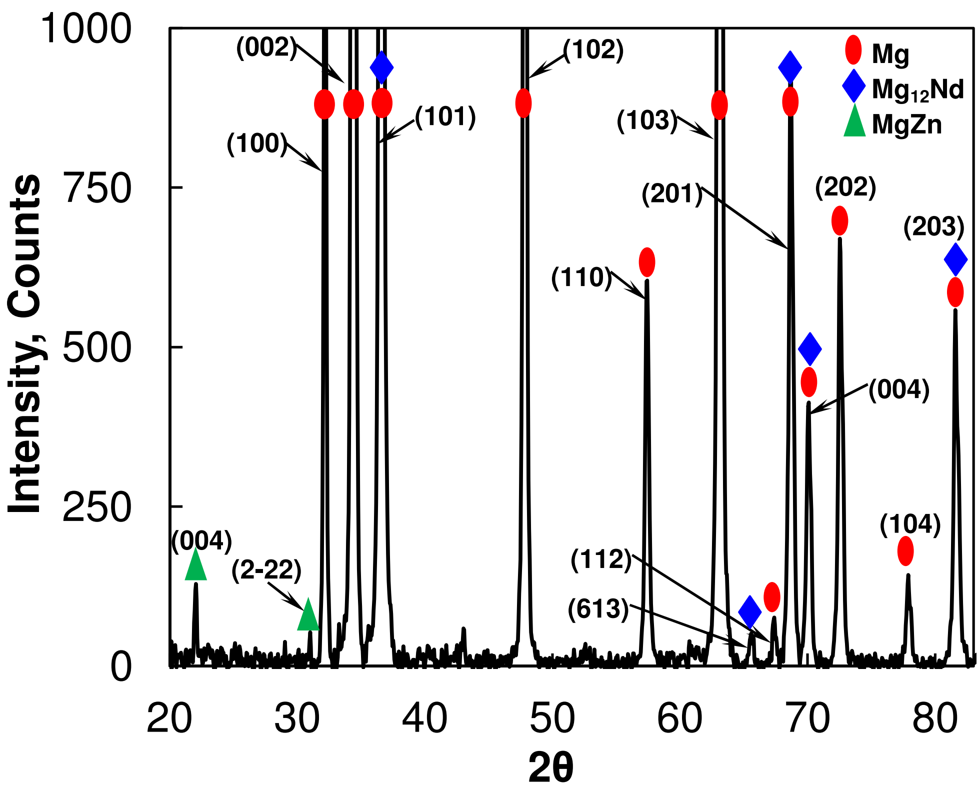

Fig.4 X-ray diffraction pattern of the ZEK100 Mg alloy.

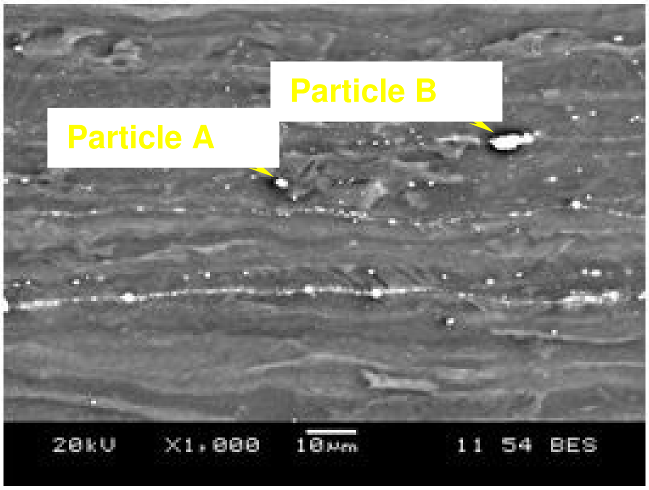

Particle A		
Element	Weight %	**Atom %**
Mg	64.9 %	**91.6 %**
Nd	35.1 %	**8.4%**

Particle B		
Element	Weight %	**Atom %**
Mg	32.3 %	**56.2 %**
Zn	67.7%	**43.8%**

Fig.5 SEM back-scattered electron image specifying EDS point analysis locations and the corresponding composition at particles A and B, respectively.

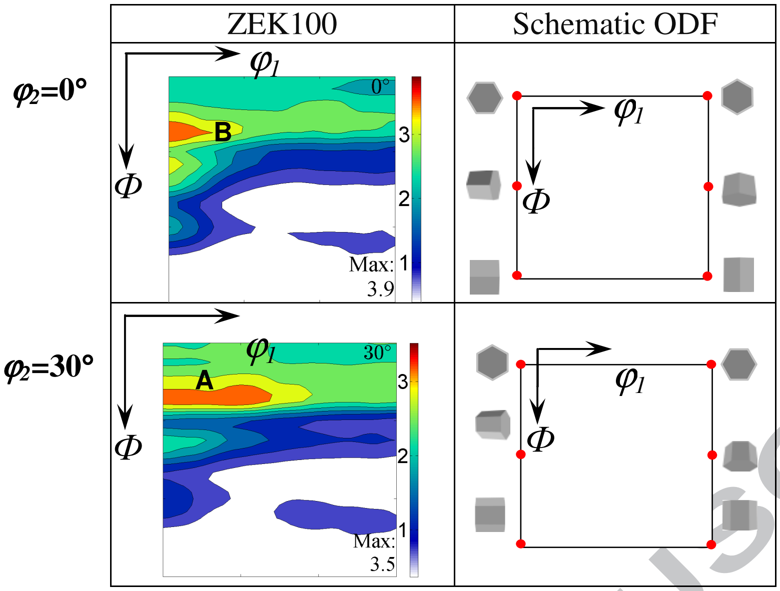

Fig.6 ODF sections at φ_2=0° and φ_2=30° of the ZEK100 Mg alloy.

Euler angles (ϕ_1 Φ ϕ_2)	**$\{hkil\}\langle uvtw\rangle$**
A (0, 25, 30)	$\{0001\}\langle 2\bar{1}\bar{1}0\rangle$
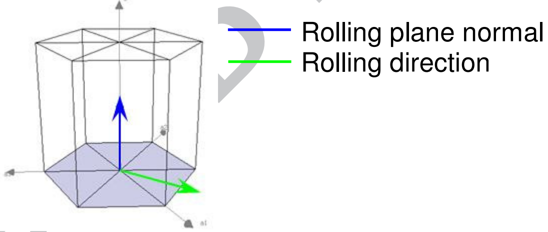 Rolling plane normal Rolling direction	
B (0, 25, 0)	$\{0001\}\langle 10\bar{1}0\rangle$
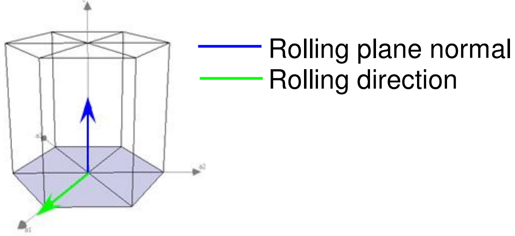 Rolling plane normal Rolling direction	

Fig.7 Main texture components A and B identified from the Euler angles.

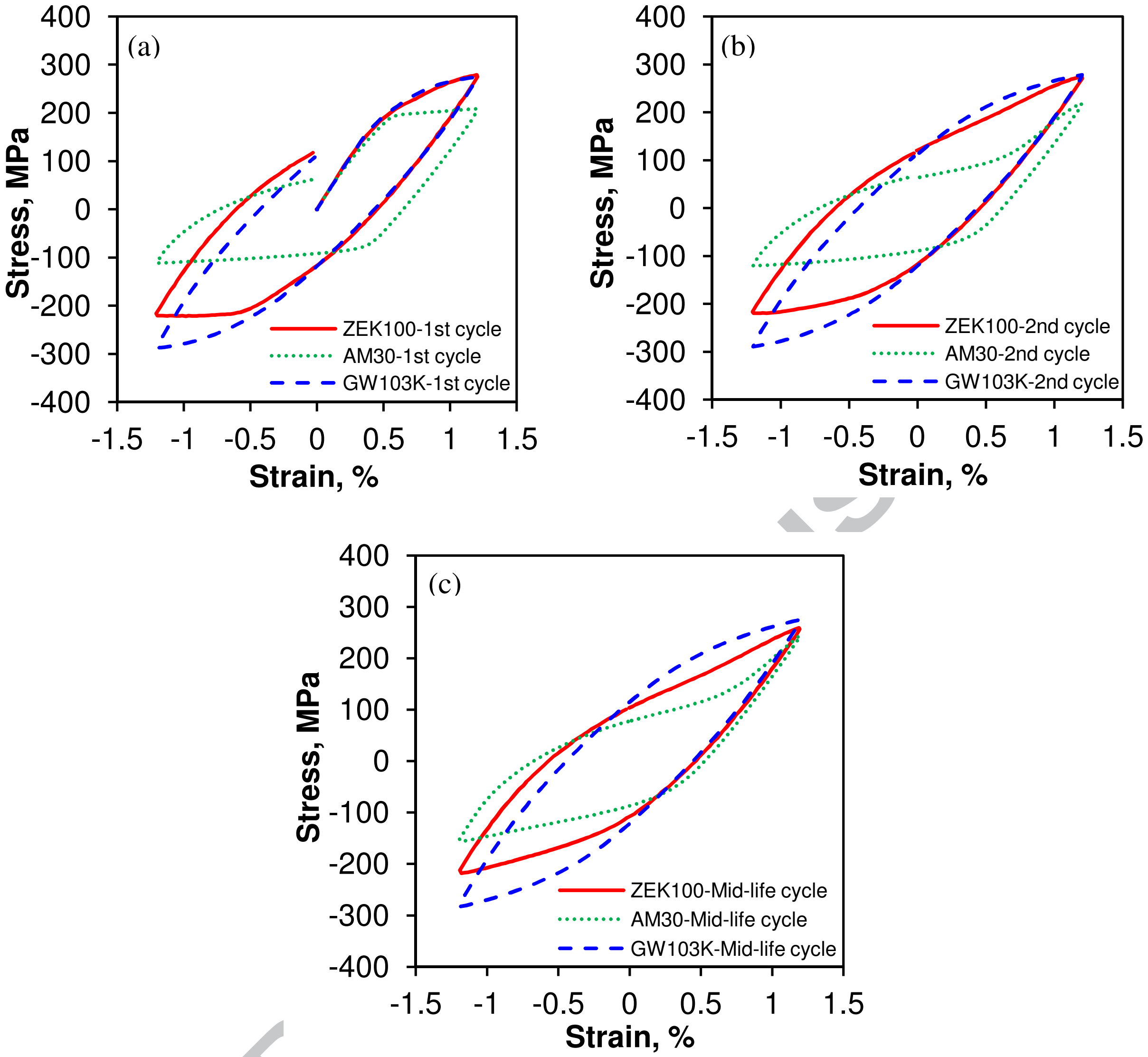

Fig.8 Characteristic stress-strain hysteresis loops of the (a) first cycle, (b) second cycle, and (c) mid-life cycle at a total strain amplitude of 1.2% and strain ratio R_s=−1 for the rolled ZEK100 alloy, in comparison with the extruded AM30 and GW103K alloys [18,21].

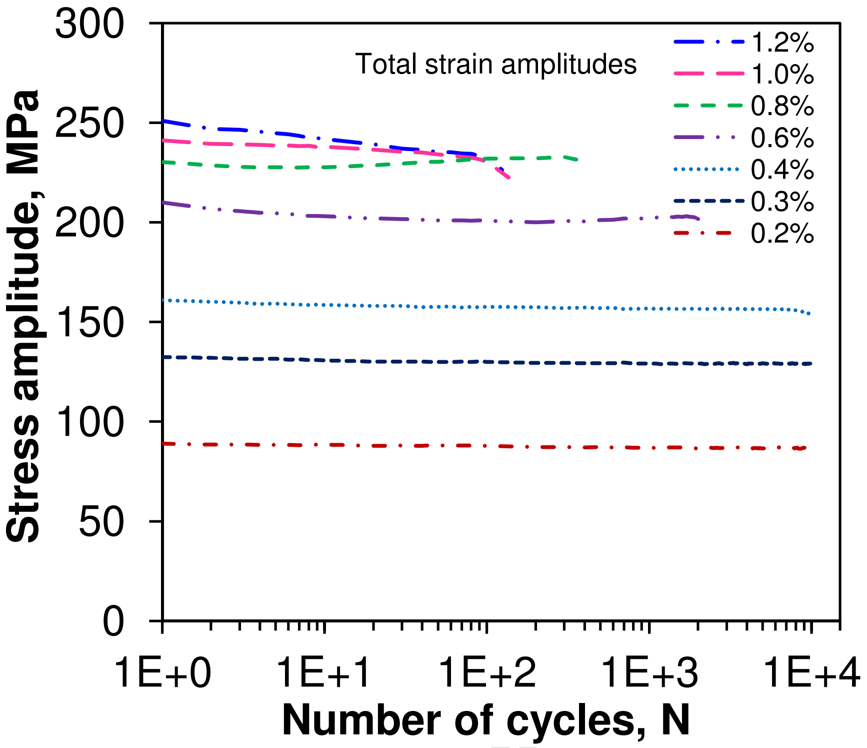

Fig.9 Stress amplitude vs. the number of cycles at different total strain amplitudes.

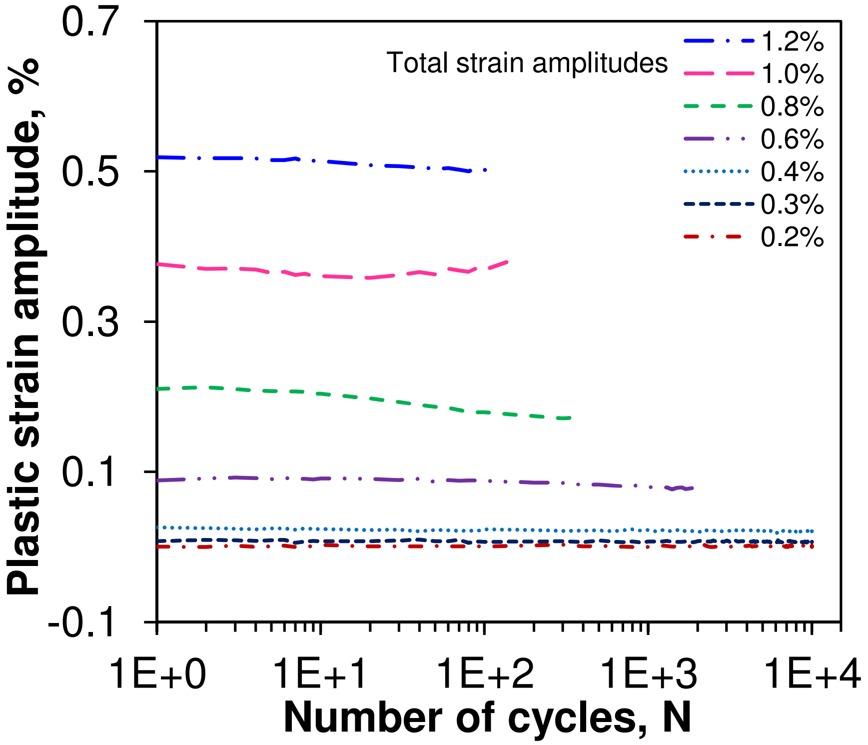

Fig.10 Plastic strain amplitude vs. the number of cycles at different total strain amplitudes.

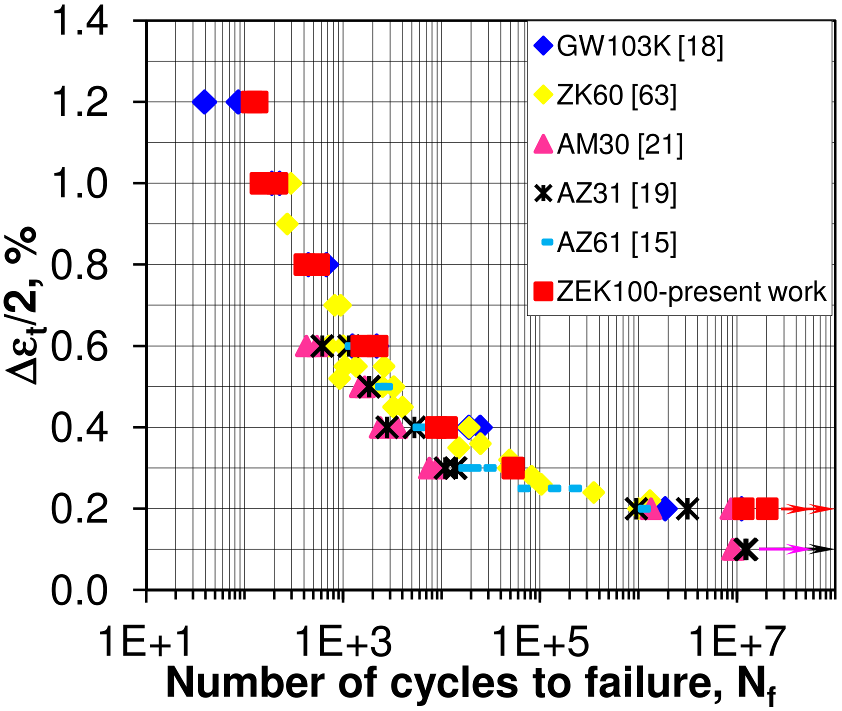

Fig.11 Total strain amplitude as a function of the number of cycles to failure for the rolled ZEK100 Mg alloy, in comparison with the data reported in the literature for various wrought Mg alloys.

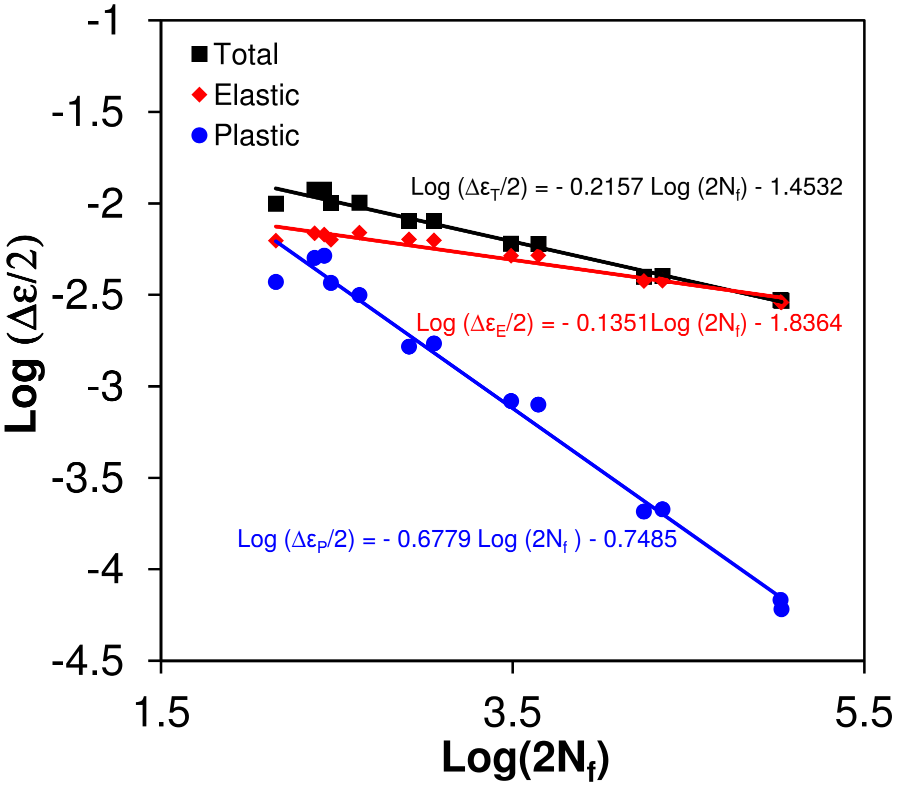

Fig.12 Evaluation of strain-life fatigue parameters in the form of log-elastic, plastic and total strain amplitudes vs. log-number of reversals to failure, respectively.

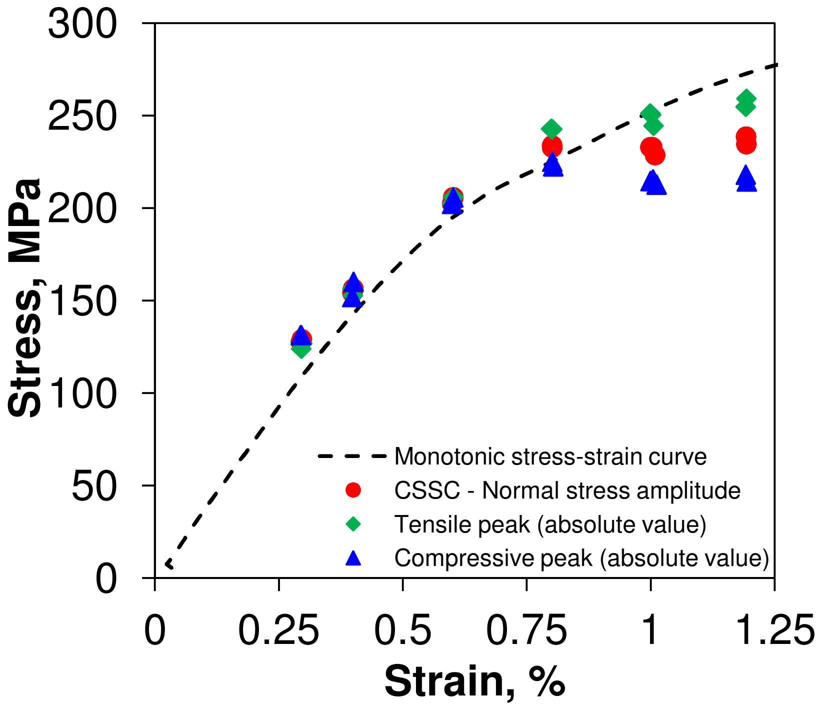

Fig.13 Cyclic stress-strain curves (CSSC) at mid-life cycles at a strain ratio of R_s=−1 in the ZEK100 Mg alloy.

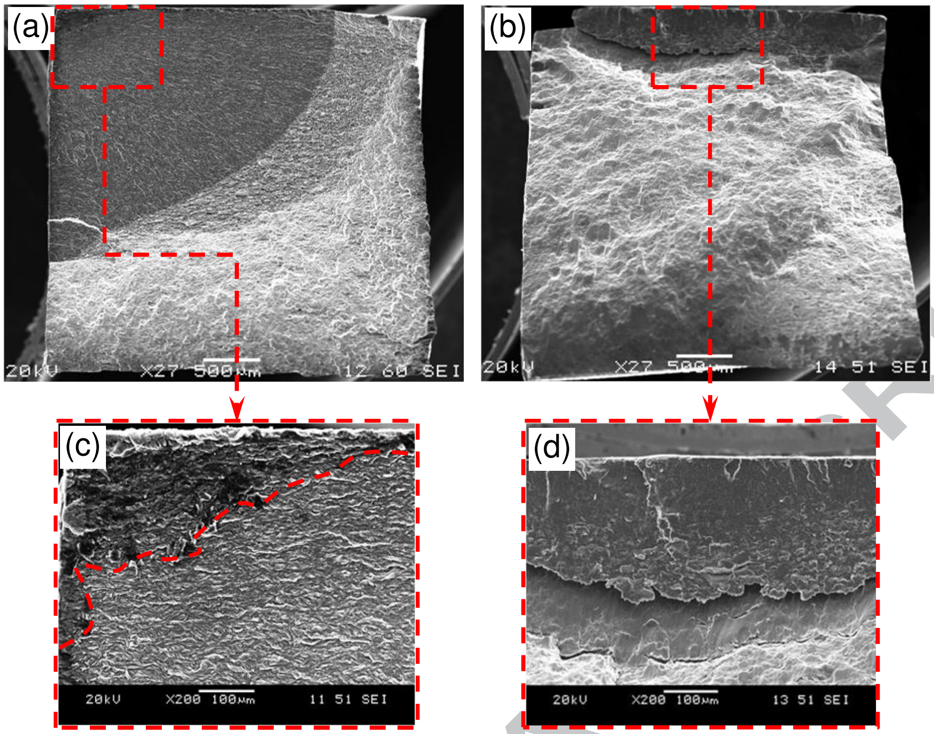

Fig.14 SEM micrographs of overall fracture surfaces of the specimens fatigued at a strain amplitude of (a) 0.4% and (b) 1.0%, respectively, and near crack initiation area at (c) 0.4% and (d) 1.0% as well.

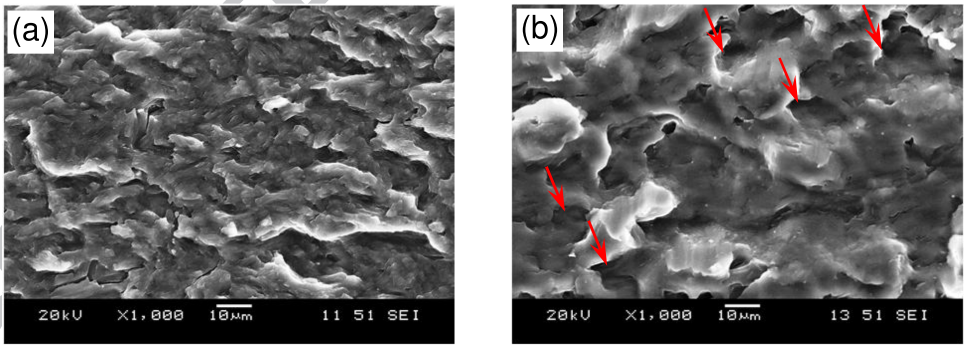

Fig.15 SEM micrographs of the fatigue crack propagation area in the specimens fatigued at a strain amplitude of (a) 0.4% and (b) 1.0%, respectively.

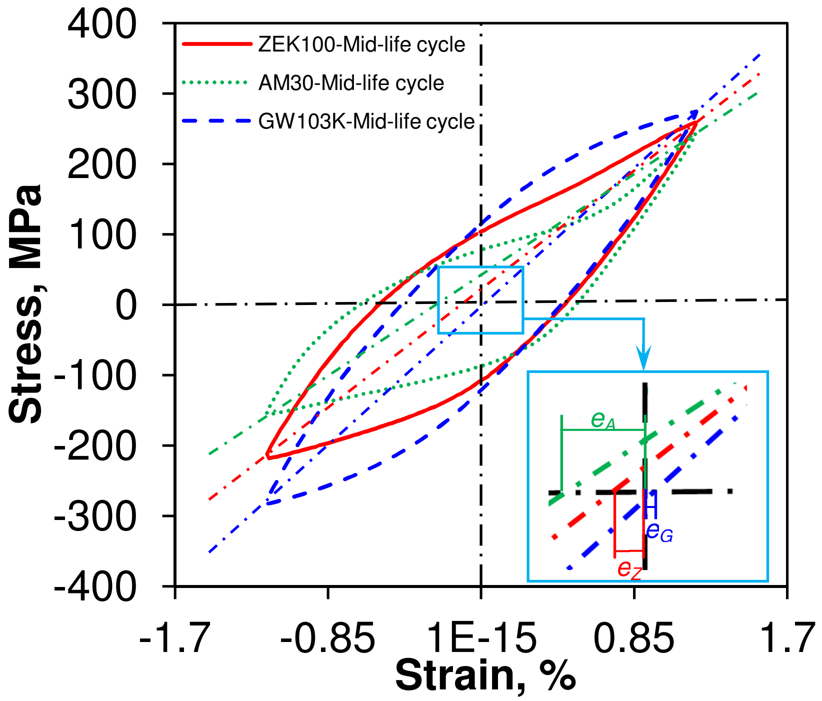

Fig.16 Stress-strain hysteresis loops of mid-life cycles at a total strain amplitude of 1.2% and a strain ratio R_s=−1 for the rolled ZEK100, extruded AM30 and GW103K alloys, respectively, showing the definition of eccentricity values of these alloys along the strain axis.

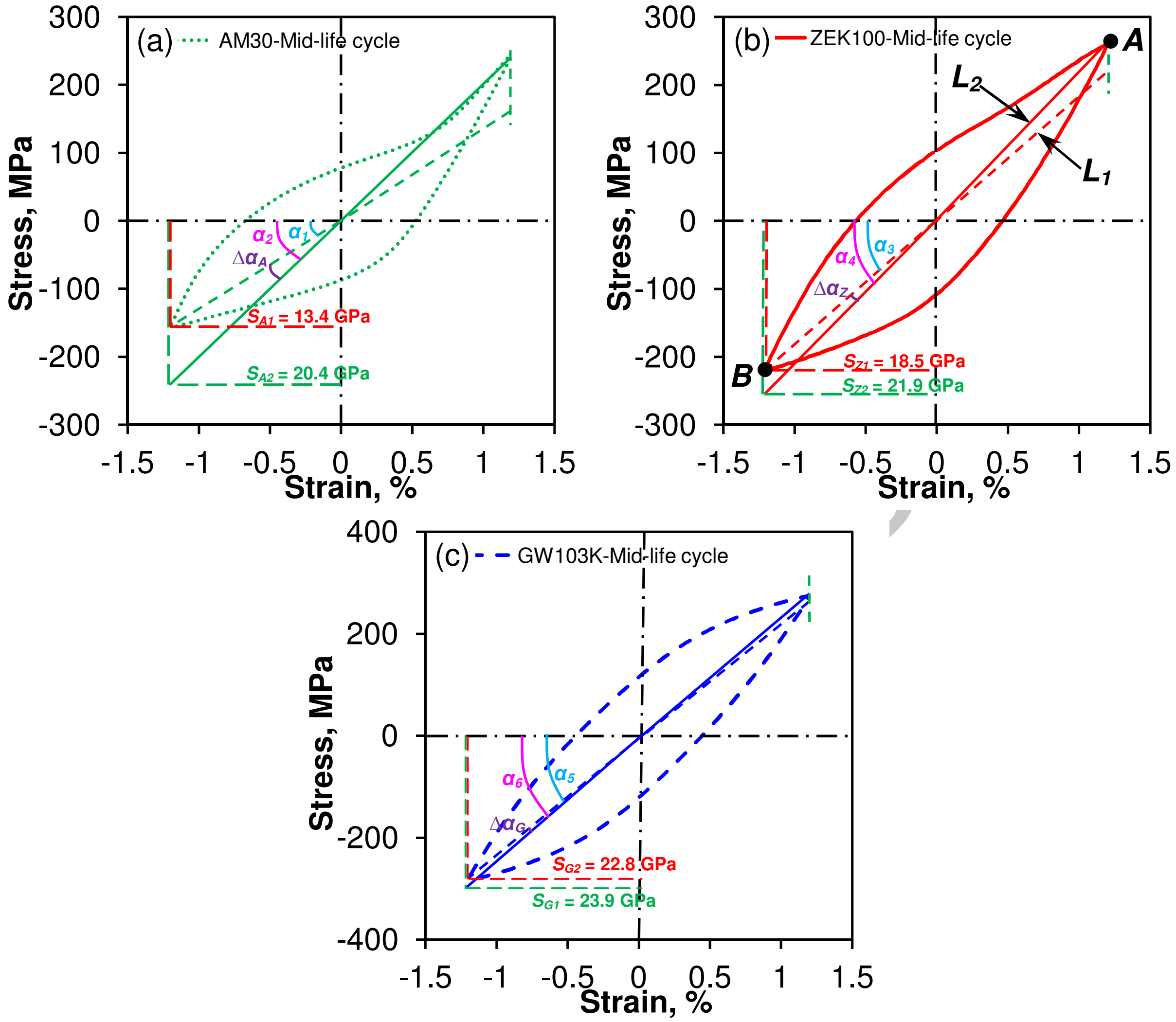

Fig.17 Stress-strain hysteresis loops of mid-life cycles at a total strain amplitude of 1.2% and strain ratio of R_s=−1 for (a) extruded AM30, (b) rolled ZEK100, and (c) GW103K alloys, respectively, showing the parameters of slope change and angle deviation.

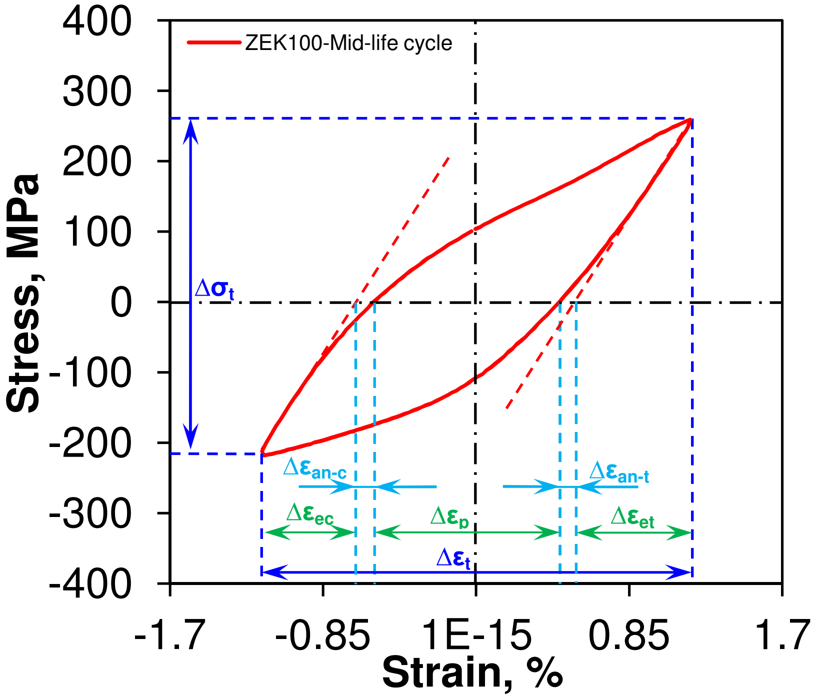

Fig.18 Stress-strain hysteresis loop of mid-life cycle at a total strain amplitude of 1.2% and strain ratio of $R_s = -1$ for the rolled ZEK100 Mg alloy, illustrating the anelastic behavior in tension and compression separately.

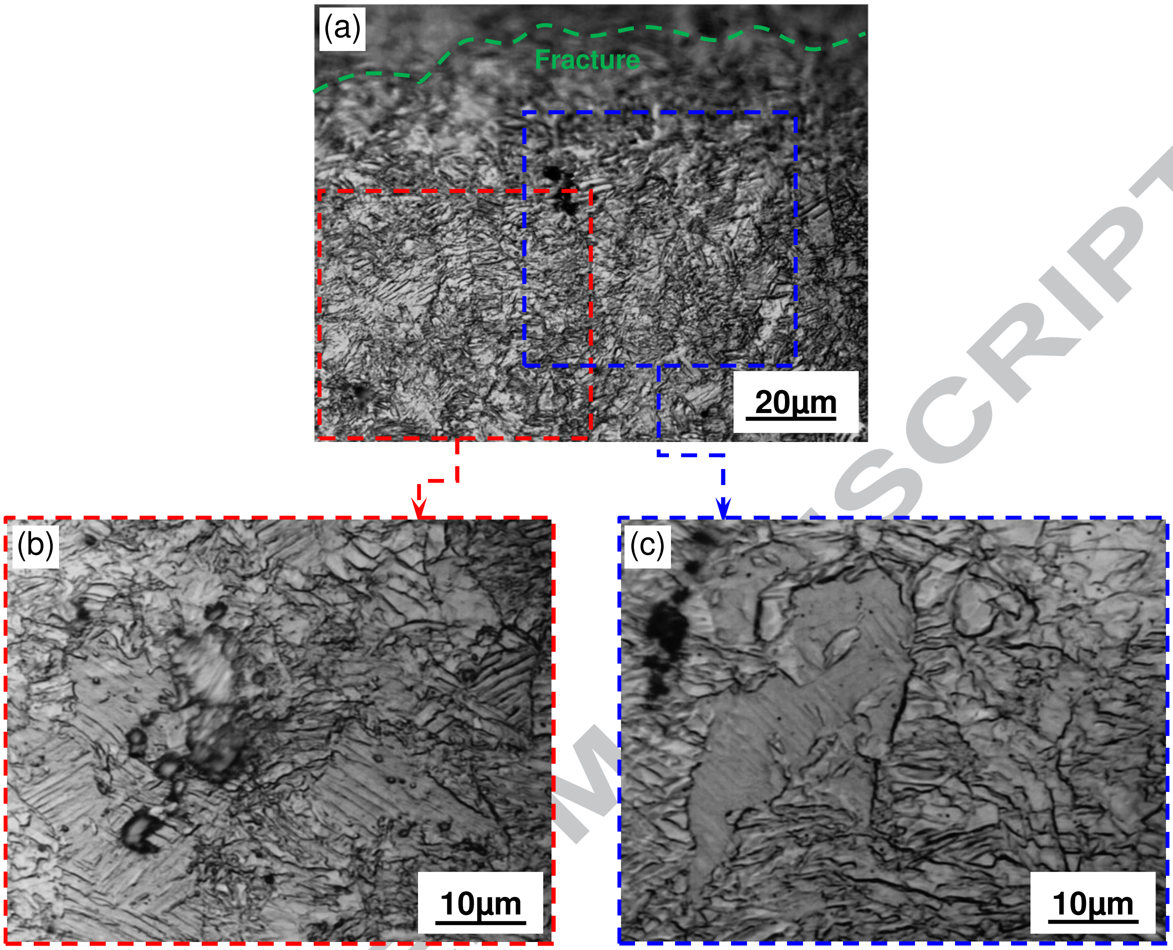

Fig.19 (a) Optical micrographs of the areas near the fracture surface, showing the overall distribution of residual twins in a sample of ZEK100 alloy fatigued at a strain amplitude of 1.2% with emphasis on two regions (b) and (c), respectively.

Research Highlights

- Low (0.2 wt.%) Nd-containing ZEK100 alloy exhibits a relatively weak basal texture.
- Cyclic stabilization sustains at lower strain amplitudes.
- Longer fatigue life is obtained for this alloy than for rare earth-free Mg alloys.
- Asymmetry and skewness of hysteresis loops are quantified through three parameters.
- Pseudo-elastic behavior still remains in the Mg alloy despite rare earth additions.